

How size and trigger matter: analyzing rainfall- and earthquake-triggered landslide inventories and their causal relation in the Koshi River basin, Central Himalaya

Jianqiang Zhang^{1,2}, Cees J. van Westen², Hakan Tanyas², Olga Mavrouli², Yonggang Ge¹, Samjwal Bajrachary³,
Deo Raj Gurung³, Megh Raj Dhital⁴, Narendral Raj Khanal⁵

¹Key Laboratory of Mountain Hazards and Surface Process/Institute of Mountain Hazards and Environment, Chinese Academy of Sciences, Chengdu, China.

²Faculty of Geo-Information Science and Earth Observation (ITC), University of Twente, the Netherlands.

³International Centre for Integrated Mountain Development (ICIMOD), Lalitpur, Nepal.

⁴The Department of Geology, Tri-Chandra Multiple Campus, Ghantaghar, Kathmandu, Nepal.

⁵Central Department of Geography, Tribhuvan University, Kathmandu, Nepal.

Correspondence to: Jianqiang Zhang(zhangjq@imde.ac.cn)

Abstract: Inventories of landslides caused by different triggering mechanisms, such as earthquakes, extreme rainfall events or anthropogenic activities, may show different characteristics in terms of distribution, contributing factors and frequency-area relationships. The aim of this research is to study such differences in landslide inventories, and the effect they have on landslide susceptibility assessment. The study area is the watershed of the trans-boundary Koshi River in central Himalaya, shared by China, Nepal and India. Detailed landslide inventories were generated based on visual interpretation of remote sensing images and field investigation for different time periods and triggering mechanisms. Maps and images from the period 1992 to 2015 were used to map 5,858 rainfall-triggered landslides and after the 2015 Gorkha earthquake, an additional 14,127 co-seismic landslides were mapped. A set of topographic, geological and land cover factors were employed to analyze their correlation with different types and sizes of landslides. The frequency-area distributions of rainfall- and earthquake-triggered landslides have similar cutoff value and power-law exponent, although the ETL might have a larger frequency of smaller one. Also topographic factors varied considerably for the two triggering events, with both altitude and slope angle showing significantly different patterns for rainfall-triggered and earthquake-triggered landslides. Landslides were classified into two size groups, in combination with the main triggering mechanism (rainfall- or earthquake-triggered). Susceptibility maps for different combinations of landslide size and triggering mechanism were generated using logistic regression analysis. The different triggers and sizes of landslide data were used to validate the models. The results showed that susceptible areas for small and large size rainfall- and earthquake-triggered landslides differed substantially.

Key words: landslides, rainfall-triggered, earthquake-triggered, frequency-area analysis, susceptibility assessment, Nepal

35 **1. Introduction**

36 Landslides are one of the most harmful geological hazards causing substantial fatalities and loss of property
37 worldwide, affecting settlements, agriculture, transportation infrastructure and engineering projects (Dilley et al. 2005;
38 Petley, 2012; Zhang et al., 2015; Haque et al., 2016). Among the various characteristics that determine the potential
39 damage of landslides, size plays an important role, as well as velocity, depth, impact pressure, or displacement which
40 differs for the various mass movement types. Volume may be an even more important landslide characteristic than size,
41 but this is difficult to measure as it requires specific geophysical or geotechnical methods that can be applied at a site
42 investigation level, or the use of multi-temporal Digital Elevation Models (SafeLand, 2015; Martha et al., 2017a).
43 Therefore, empirical relations between landslide area and volume are generally used (Hovius et al, 1997; Dai and Lee,
44 2001; Guzzetti et al., 2008; Larsen et al., 2011; Klar et al., 2011; Larsen and Montgomery, 2012). To investigate
45 whether earthquake- and rainfall-triggered landslides inventories have similar area-frequency distributions, area-
46 volume relations and spatially controlling factors, it is important to collect event-based landslide inventories. The
47 difficulty is to collect complete inventories that are independent for earthquakes and rainfalls in same study area.

48 The quality of a landslide inventory can be indicated by its accuracy, which refers to the correctness in location and
49 classification of the landslides, and its completeness, which measures how many of the total number of landslides in
50 the field were actually mapped (Guzzetti et al., 2012). The accuracy and completeness have a large influence on the
51 quality and reliability of the susceptibility and hazards maps that are either using the inventory as input (e.g. in
52 statistical modelling) and in validation (e.g. statistical and physically-based modeling) (Li et al., 2014). There are
53 several explanations why landslide inventories differ in frequency-area distribution, such as the under sampling of
54 small slides (Stark and Hovius, 2001), or the amalgamation, the merging of several landslides into single polygons
55 (Marc and Hovius 2015).

56 Landslides might be triggered by various processes, among which anthropogenic activities, volcanic processes, sudden
57 temperature changes, earthquakes and extreme rainfall (Highland and Bobrowski, 2008). The latter two are the most
58 frequently occurring, and causing the highest number of casualties (Keefer, 2002; Petley, 2012; Kirschbaum et al,
59 2015; Froude and Petley, 2018). Comparing landslide inventories for the same area and for the same triggering event
60 has been carried out by several authors (e.g. Pellicani and Spilotro, 2015; Tanyas et al., 2017a). Some studies took
61 independent earthquake- and rainfall-triggered landslide inventories to compare the characteristics of landslides
62 induced by different triggers. Malamud et al. (2004) compared earthquake-triggered landslides from the Northridge
63 earthquake, Umbria snowmelt-triggered landslide and Guatemala rainfall-triggered landslide as examples, and
64 concluded that the three frequency-area distributions were in good agreement with each other. Meunier et al. (2008)
65 compared earthquake-triggered landslides, from Northridge, Chi-Chi Finisterre Mountains (Papua New Guinea), to

66 evaluate topographic site effects on the distribution of landslides. Tanyas et al. (2017b) created a database with 363
67 landslide-triggering earthquakes and 64 digital landslide inventories, which were compared. The number of studies
68 that compare earthquake-triggered landslide with rainfall triggered ones for the same area is less numerous. They are
69 mostly focusing on mapping rainfall-induced landslides after an earthquake, such as for the 1999 Chi-Chi earthquake
70 (Lin et al., 2006; 2008), the 2005 Kashmir earthquake (Saba et al., 2010) or the 2008 Wenchuan earthquake (Tang et
71 al., 2010; Tang et al., 2016; Fan et al., 2018a). Fewer studies carried out on multi-temporal RTL inventories in Taiwan,
72 Papua New Guinea, Japan and Central Nepal before earthquake, which supplied good comparison study for RTL under
73 the effect and without the effect of earthquakes (Marc et al., 2015, 2019). The problem with the studies indicated above
74 is that rainfall-triggered landslides that occur shortly after a major earthquake are generally following the same spatial
75 patterns, due to the availability of large volumes of landslide materials of the co-seismic landslides (Hovius et al.,
76 2011; Tang et al., 2016; Fan et al., 2018a). However, other studies argue that there is not a clear correlation of rainfall-
77 triggered landslides with the co-seismic pattern, as only the 20- 30% of the RTL that occurred just after an earthquake,
78 are spatially related to ETL, suggesting limited re-activation of ETL by RTL (Marc et al., 2015, 2019).

79 There are very few studies that have validated landslide susceptibility maps with independent landslide inventories of
80 triggering events that occurred after the maps were produced. Chang et al. (2007) used landslides triggered by a major
81 earthquake and a typhoon prior to the earthquake to develop an earthquake-induced model and a typhoon-induced
82 model. The models were then validated by using landslides triggered by three typhoons after the earthquake.
83 According to the results, typhoon-triggered landslides tended to be near stream channels and earthquake-triggered
84 landslides were more likely to be near ridge lines. Although landslide size is often considered important in hazard and
85 risk assessment, it is generally not considered as a separate component of the susceptibility assessment. The different
86 relation with contributing factors of earthquake-triggered and rainfall-triggered landslides may also be related to the
87 size distribution (Korup et al., 2007). For instance, Fan et al. (2012) concluded that small ($<10 \times 10^4 \text{m}^3$) rainfall-
88 triggered landslide and earthquake-triggered landslides have similar runout distances, whereas for larger landslides
89 earthquake-triggered ones showed longer runouts. Peng et al. (2014) analyzed the landslides in the Three Gorges area
90 and found that different landslide sizes had different relations with contributing factors.

91 The aim of this study is to investigate the differences in the characteristics of earthquake-triggered and rainfall
92 triggered landslides in terms of their frequency-area relationships, spatial distributions and relation with contributing
93 factors, and to evaluate whether separate susceptibility maps generated for specific landslide sizes and triggering
94 mechanism are better than a generic landslide susceptibility assessment including all landslide sizes and triggers. This
95 research aims to address a number of questions related to the difference of using earthquake-induced and rainfall-
96 induced landslide inventories for the generation of landslide susceptibility maps. The question will be addressed that,
97 whether different landslide size groups are controlled by different sets of contributing factors. By extension, whether it

98 is possible to utilize inventories of earthquake-triggered landslides (ETL) as inputs for analyzing the susceptibility of
99 rainfall-triggered landslides (RTL) and vice versa.

101 **2. Study area**

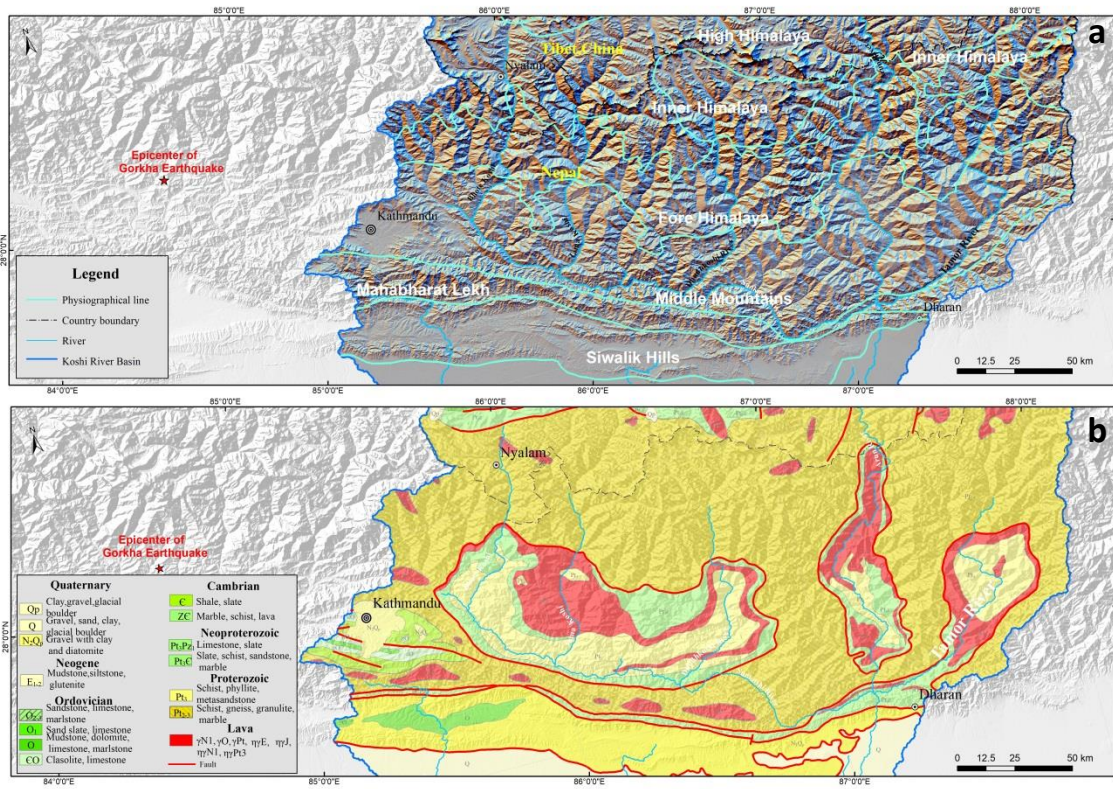
102 The study was carried out in the Koshi River basin, which is a trans-boundary basin located in China, Nepal and India
103 in the central Himalayas (Fig. 1a). The mountainous regions in the upper reaches of the basin where landslides have
104 occurred are located in China and Nepal, and the Indian part consists of relatively flat areas. The elevation of Koshi
105 River basin varies from 60 m a.s.l. at the outlet in India up to 8,844 m at the highest point at Mount Everest. The
106 Koshi basin can be classified into 6 physiographic zones from South to North: Terai, Siwalik Hills, Mahabharat Lekh,
107 Middle Mountains, High Himalaya, and Tibetan Plateau (Gurung and Khanal, 1987; Dhital, 2015). Considering the
108 distribution of landslides, the Tibetan plateau in the upper reaches and the plains in the lower reaches were excluded.

109 In the Koshi Basin, the major geological structures have an approximate east–west orientation, such as the foreland
110 thrust-fold belt, Main Central Thrust (MCT), South Tibetan Detachment System (STDS) and the Yarlung Zangbo
111 Suture Zone (YZSZ) (Gansser, 1964; Dhital, 2015). The southernmost part of the basin consists of the Quaternary
112 sediments underlain by the Neogene Siwaliks. The Siwaliks comprise soft mudstones, sandstones and conglomerates.
113 In this part of the foreland basin, a number of emergent and blind imbricate faults originate from the Main Himalayan
114 Thrust. The overlying Lesser Himalayan succession forms duplexes and imbricate stacks. The Proterozoic to Miocene
115 rocks of the Lesser Himalaya include limestones, dolomites, slates, phyllites, schists, quartzites, and gneisses (Dhital,
116 2015). A regional-scale thrust MCT separates the Lesser Himalayan sequence from the overlying Higher Himalayan
117 crystallines, which consist of medium- to high-grade metamorphic rocks (e.g., schists, quartzites, amphibolites,
118 marbles, gneisses, and migmatites) and granites aged from the Proterozoic to Miocene. The STDS delineates the
119 Higher Himalayan rocks from the overlying Tethyan sedimentary sequence of Paleozoic–Cenozoic age (Gansser, 1964;
120 Burg et al., 1984; Hodges et al., 1996) (Fig. 1b).

121 In the study area there are three main tributaries of the Koshi River: the Arun (main branch) coming from the north, the
122 Sun Koshi from the west and Tamor from the east. Nearly every year, during the monsoon period, which generally
123 lasts from June to September, the area is affected by rainfall-triggered landslides. Dahal and Hasegawa (2008) used a
124 dataset of 193 landslides occurring from 1951 to 2006, part of which were from the Koshi River basin, to generate a
125 threshold relationship between rainfall intensity, rainfall duration, and landslide initiation. The latest research from
126 Marc et al. (2019) gives the magnitude of annual landsliding in different High Himalayan valleys.

127 The area was severely affected by the Gorkha earthquake, with a moment magnitude of 7.8 on 25 April 2015. The
128 epicenter was located near Gorkha, which is about 80km west of the study area. A second major earthquake occurred
129 along the same fault on 12 May 2015 with a moment magnitude of 7.3 with the epicenter located inside the Koshi

130 River basin. The second event is considered as a major aftershock of the main Gorkha earthquake. Both events
 131 triggered many landslides (Collins and Jobson, 2015; Kargel et al., 2016; Zhang et al., 2016; Martha et al., 2017b).
 132



133 **Fig. 1** Maps showing the study area (a) Physiographic zones of the Koshi River basin; (b) Geological map showing the
 134 main geological zones (Dhital, 2015; Zhang et al., 2016).
 135
 136

137 3. Input data

138 The study requires a series of landslide inventory maps, and contributing factor maps, which were generated for the
 139 middle part of the Koshi basin, where most of the landslides were concentrated. Two landslide inventories were
 140 generated: a pre-2015 inventory showing rainfall-triggered landslides, and a co-seismic landslide map for the 2015
 141 Gorkha earthquake. The pre-2015 inventory map was generated using topographic maps, multi-temporal Google Earth
 142 Pro images and Landsat ETM/TM images. We were able to digitize landslide polygons from the available 1:50,000
 143 scale topographic maps, which cover only the Nepalese part of the Koshi River basin. These maps were generated
 144 from aerial photographs acquired in 1992, and active landslides with a minimum size of 450 m² visible on these
 145 images were marked as separate units. The landslides could not be separated in initiation and accumulation zones, and

146 also no classification of landslide types could be done, as this was not indicated on the topographic maps. A set of pre-
147 2015 Landsat ETM/TM images were available for the entire study area, from which the post 1992 and pre-2015
148 landslides. Pre-2015 landslides were also mapped from historical images using Google Earth Pro Historical Imagery
149 Viewer which contains images from 1984 onwards. Although the oldest images are Landsat images, the more recent
150 ones have much higher resolution, although not covering the whole study area in equal level of detail. By comparing
151 the different images for the period between 1992 and 2015 we were able to recognize most of the landslides. We
152 carried out field verification for a number of samples (Fig. 2). Images from Google Earth were downloaded and geo-
153 referenced and landslides were mapped using visual image interpretation and screen digitizing. A total of 5,858 rainfall
154 induced landslides were identified in the Koshi River basin. This inventory has a limitation that, landslide occurred and
155 revegetated during 1992 and 2015 could not be identified by the remote sensing images obtained in 2015. It is
156 impossible to make a complete historical landslide inventory in this region due to lack of multi-temporal high
157 resolution images (Marc et al., 2019).



158
159 Fig. 2 Field investigation on landslide in Koshi river basin (a) Jury landslide triggered by rainfall occurred on August 2,
160 2014 at Sunkoshi river(photo by Bintao Liu in 2017); (b) Small size of landslides triggered by Gorkha earthquake in
161 Bhotekoshi watershed.

162
163 After the 2015 April 25th Gorkha earthquake, a substantially complete earthquake-triggered landslide inventory was
164 created by Roback et al. (2017). They mapped landslides using high-resolution (<1m pixel resolution) pre- and post-
165 event satellite imagery. In total 24,915 landslide areas were mapped, of which 14,022 landslides were located in the
166 Koshi river basin. Chinese GaoFen-1 and GaoFen-2 satellites imageries (with 2.5m resolution) of the CNSA (China
167 National Space Administration), which are part of the HDEOS (High-Definition Earth Observation Satellite) program,
168 were employed to validate this landslide inventory. These images were captured during 27 April, 2015 to May 14 2015.
169 Finally 15 landslide polygons were deleted, and 120 landslides were added to the inventory.

170 For the susceptibility assessment, we extracted the point located in the highest part of the landslides, as indicative of
171 the initiation conditions. Different DEMs, such as ASTER GDEM, SRTM Digital Elevation Model with both 90 m and
172 30m spatial resolution, as well as ALOS PALSAR DEM were evaluated to use in this study. After careful analysis
173 however, both ASTER GDEM and 30m SRTM contained many erroneous data points, ALOS PALSAR DEM with
174 highest resolution of 12.5m, was utilized in this study. ESRI ArcGIS software enabled the calculation of topographical
175 factors including slope gradient, aspect, and curvature. Streams and gullies were obtained through DEM processing,
176 and the drainage density was calculated. The land cover dataset GlobeLand30 with 30×30 m spatial resolution,
177 developed by the National Geomatics Center of China, was employed in this study. The land cover types include
178 cultivated land, forest, grassland, shrub land, wetland, water bodies, tundra, artificial surfaces and bare land.
179 Geological maps of Nepal, and Tibet were obtained from Chengdu Geological Survey Center of the China Geological
180 Survey. The Peak Ground Acceleration data for the Gorkha earthquake were obtained from USGS Shakemap, which
181 was designed as a rapid response tool to portray the extent and variation of ground shaking throughout the affected
182 region immediately following significant earthquakes (Wald et al., 1999). Given the rather low resolution of the input
183 data, the relation with landslides as small as 50m^2 may not be optimal, especially also considering the rather long time
184 period over which land cover changes have occurred in many areas. But given the regional scale of this analysis, the
185 use of higher resolution data was unfortunately not a viable option.

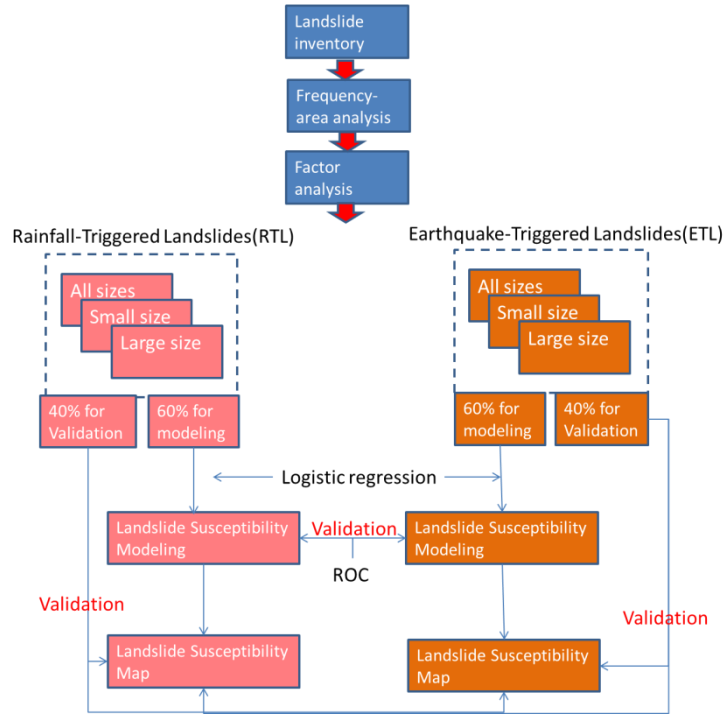
186

187 **4. Methods**

188 Figure 3 gives an overview of the method followed in this study. The landslide inventories were subdivided into
189 training and test datasets. It is a generally accepted method in literature to separate the landslide dataset into a training
190 and validation set (e.g. Hussin et al. 2016; Reichenbach et al., 2018), although the separation thresholds differs among
191 authors. We decided to select 60% of the landslide data as training data for the modeling, and 40% for the validation.
192 We examined the frequency-area distribution of the gathered inventories using the method described by Clauset et al.
193 (2009). They proposed a numerical method to identify the slope of power-law distribution (β) and the point where
194 frequency-area distribution diverges from the power-law (cutoff point).

195 Based on the frequency area distribution the RTL and ETL inventories were separated in two size-groups each. Initially
196 bivariate statistical analysis was used for the different types and sizes of landslides, to investigate the correlation
197 between landslides with contributing factors. After selecting the relevant factors, the logistic regression method was
198 used to build the susceptibility model for each size group. The Logistic Regression method is the most commonly used
199 model in landslide susceptibility assessment (Ayalew and Yamagish, 2005; Bai et al., 2010; Das et al., 2000; Nandi and
200 Shakoor, 2010; Wang et al., 2013). For the susceptibility modeling of RTL, the following factors were used: altitude
201 (x_1), slope gradient (x_2), curvature (x_3), slope aspect (x_4), relative relief (x_5), drainage density (x_6), lithology (x_7),

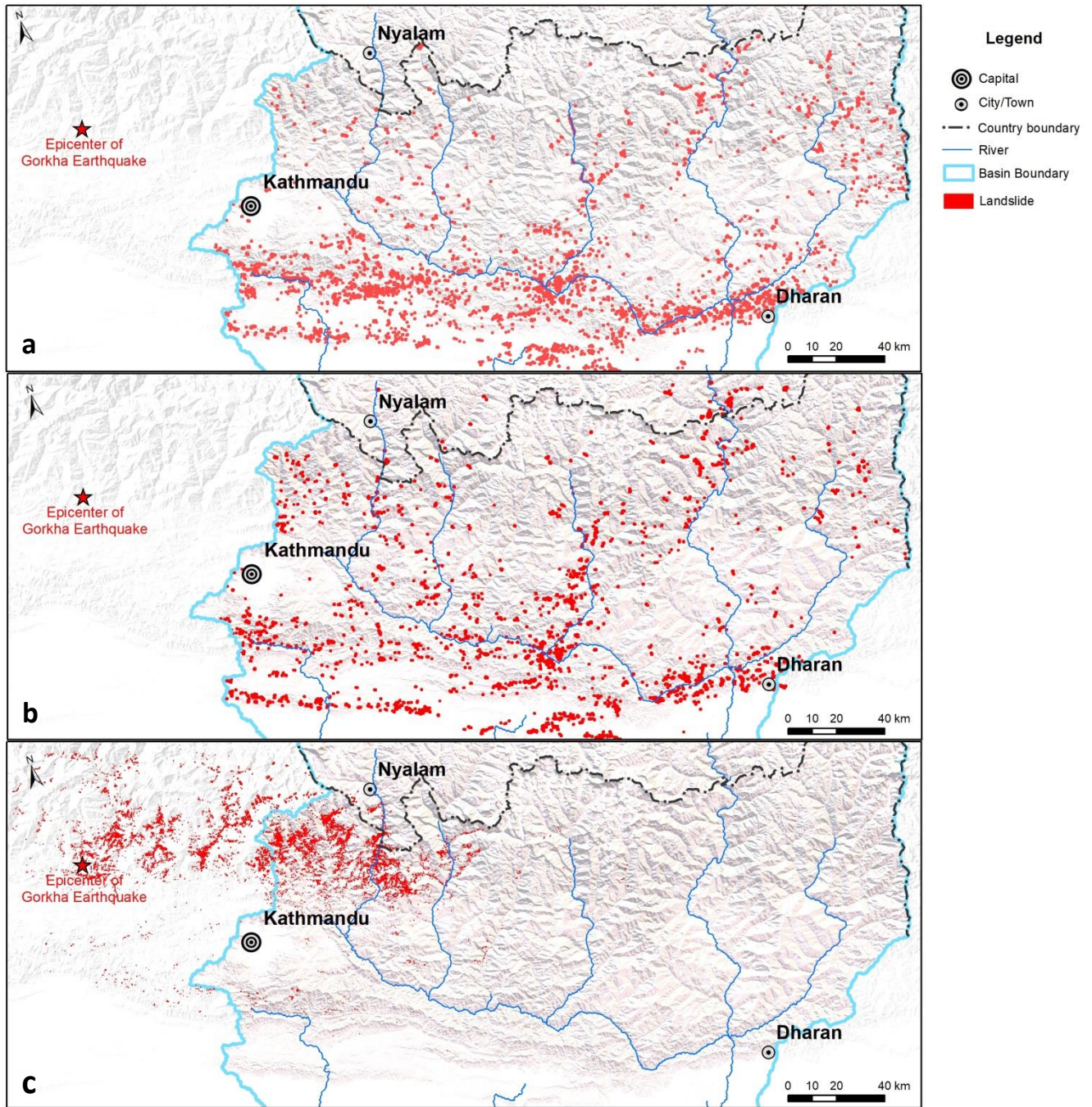
202 distance to faults (x_8), land cover type (x_9), precipitation during monsoon(x_{10}). For the susceptibility modeling of ETL,
 203 precipitation during monsoon(x_{10}) was instead of peak ground acceleration (x_{10}). The statistical software R developed
 204 at Bell Laboratories was used to build the models for different types and sizes of landslide respectively. ROC (Receiver
 205 Operating Characteristic) curves (Fawcett, 2006) were used to verify the accuracy of the susceptibility models, and
 206 finally six landslide susceptibility maps were generated and compared (Fig. 3).



207
 208 **Fig. 3** Methodology for susceptibility assessment to different types and sizes of landslide
 209

210 5. Landslide characteristics

211 In the Koshi River basin, a total of 5,858 RTL were mapped. The Gorkha earthquake triggered more than 25,020
 212 landslides, of which 14,127 were located in the Koshi River basin. Landslide characteristics were analyzed based on
 213 frequency-area distribution and factor statistics (Fig. 4).



214
 215 **Fig. 4** Landslide inventories of the Koshi River basin (a) Rainfall induced landslide inventory of events before 1992; (b)
 216 Rainfall induced landslide inventory for the period between 1992 to 2015; (c) Inventory of landslides triggered by the
 217 2015 Gorkha earthquake(Roback et al. 2017).

218 5.1 Landslide frequency-area distributions

219 Size statistics of landslides are analyzed using frequency-area distribution curves of landslides (e.g., Malamud et al.,
220 2004). There is a large literature arguing that frequency-area distribution of medium and large landslides has power-
221 law distribution, which diverges from power-law towards smaller sizes (e.g., Hovius et al., 1997, 2000; Malamud et
222 al., 2004). Given this argument, we can identify the divergence point of frequency-area distribution curve to determine
223 a site specific threshold values referring to the limit between medium and small landslides.

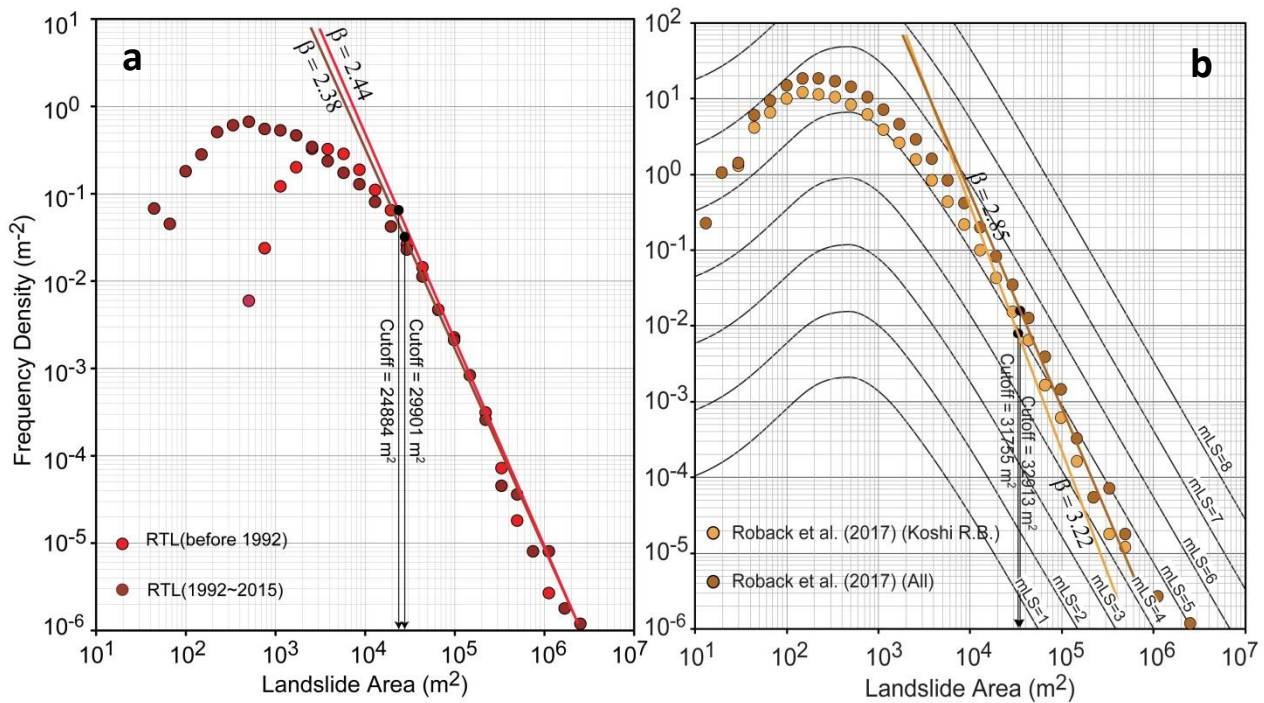
224 The frequency-area distributions (FAD) of landslides were separately analyzed for both RTL and ETL inventories (Fig.
225 5). For the RTL both landslide inventory datasets of before 1992 and 1992~2015 were analyzed (Fig. 5a). For the ETL
226 of the Gorkha earthquake, landslides located in the Koshi River basin were analyzed separately from the entire
227 landslide-affected area. We obtained similar β values for the RTL triggered before 1992 ($\beta = 2.44$) and triggered from
228 1992 to 2015 ($\beta = 2.38$) (Fig. 5a). On the other hand, we observe larger differences between the β values obtained for
229 ETL inventories created for both Koshi River basin and entire landslide-affected area (Fig. 5b).

230 We also examine the cutoff values of inventories. The historical RTL inventories and ETL inventory that we examined
231 for both Koshi River basin and entire landslide-affected area gave similar cutoff values changing from 24,884 m² to
232 32,913 m² (Fig. 5). This finding shows that, the limit between small and large landslides are consistently obtained from
233 these inventories about 30,000 m². Given this finding, the proposed landslide size classification system of China the
234 Tong et al. (2013) seems like an acceptable approach for our study area. They proposed a classification with landslides
235 with an area smaller than 10,000 m² as small, those with an area between 10,000 m² and 100,000 m² as medium, and
236 those with larger sizes than 100,000 m² as large size landslide. Considering this study, and the cutoff values calculated
237 in our study, 30,000 m² was picked as a threshold value for large landslides.

238

239

240



241

242 **Fig. 5** Landslide frequency - area distributions of (a) RTL inventories, (b) ETL inventories created for Koshi River basin
 243 and ETL inventories created for the entire landslide-affected area of the 2015 Gorkha, Nepal earthquake (Roback's
 244 landslide inventory was validated). Cutoff and β values are calculated using the method proposed by Clauset et al.
 245 (2009).

246

247 Based on the results of the FAD analysis, that resulted in similar cutoff values for the RTL and ETL and similar β
 248 values, we subdivided them into two size-groups, with 30,000 m² as threshold value (Table 1). The results will
 249 therefore be more reliable for the class above the threshold of 30,000 m², where under sampling is not an issue, then
 250 for the small landslide class, which has different rollover points, and completeness levels.

251

252

Table 1 Numbers for different types and sizes of landslide in Koshi River basin

	Rainfall-triggered landslides (RTL)			Earthquake-triggered landslides (ETL)		
	All sizes	Small size	Large size	All sizes	Small size	Large size
Total	5,858	5267	591	14,127	13981	146
Modelling	3,515	3160	355	8476	8388	88
Validation	2,343	2107	236	5650	5593	58

254 5.2 Correlation of landslides with contributing factors

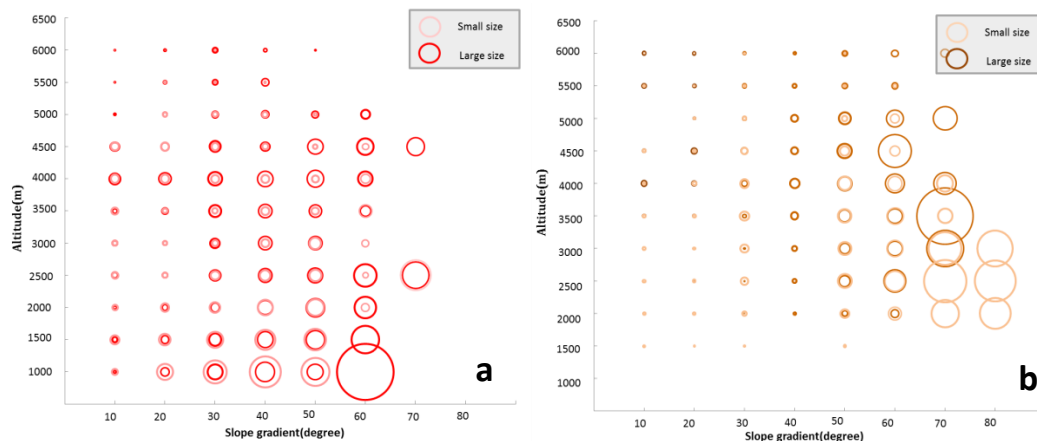
255 In order to evaluate their relation with landslide occurrence the factor maps were analyzed using the Frequency Ratio
 256 method (Razavizadeh et al., 2017).

$$257 \text{FR} = \frac{E/F}{M/L}$$

258 where E is the area of landslides in the conditioning factor group, F is the area of landslides in the entire study area, M
 259 is the area of the conditioning factor group, and L is the entire study area. The analysis was carried out for different
 260 triggers and size groups, and each time two factors were combined (e.g. altitude with slope gradient, altitude with slope
 261 direction, lithology with slope gradient). The results are summarized in Fig. 6. Fig. 6a&b show that rainfall triggered
 262 landslides (RTL) are more frequent in low altitude areas than earthquake triggered landslides (ETL). However, it is
 263 important to keep in mind that the ETL is an event inventory of a single earthquake, where the epicenter was located at
 264 higher altitude (See Fig. 4) and the RTL is a multi-temporal inventory, showing the accumulated inventory of many
 265 individual events.

266 Fig. 6 c&d show the relation with slope and lithology. RTLs are concentrated on Proterozoic metamorphic lithological
 267 units (Pt3), consisting of schist, phyllite and metasandstone, and in Quaternary molasse (N2Qp) units, consisting of
 268 gravel and clay (See Fig. 1). ETLs are linked to units consisting of shale and slate (Pt3e), and Cambrian units
 269 consisting of shale and slate (e) and marble, schist and lava (Ze).

270



271
 272
 273

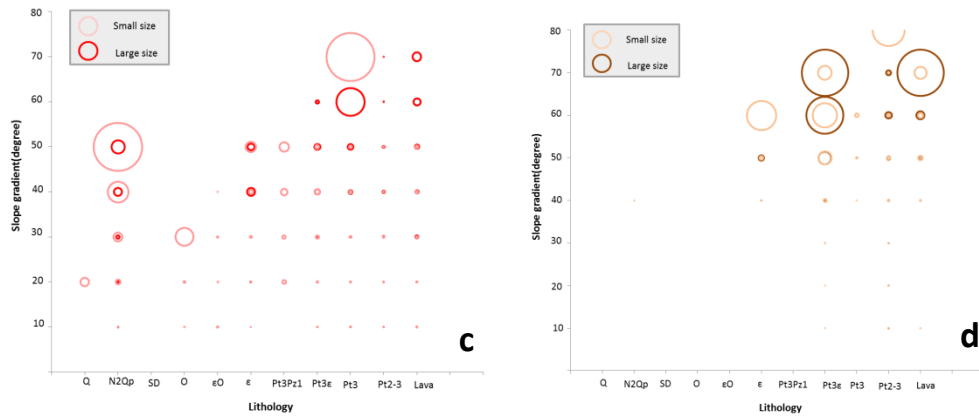


Fig. 6 Correlation between landslides and other factors for rainfall triggered landslides (RTL) on the left side, and earthquake-triggered landslides (ETL) on the right side. The size of the circles indicate the value of the Frequency Ratio. a & b: Relation between altitude and slope gradient; c & d: Relation between Lithology and slope gradient.

6. Landslide susceptibility assessment

6.1 Landslide susceptibility models

The following factors were used for the susceptibility modeling of RTL: altitude(x_1), slope gradient(x_2), curvature(x_3), slope aspect(x_4), relative relief(x_5), drainage density(x_6), lithology(x_7), distance to fault(x_8), land cover type(x_9) and precipitation during monsoon(x_{10}). Peak Ground Acceleration (PGA) was used instead of precipitation for the susceptibility modeling of ETL (Fig. 7). The R software was used to build the models by Logistic Regression method for different types and sizes of landslide respectively (Table 2). ROC curves were generated to verify the accuracy of each susceptibility model, and value of the Area Under Curve (AUC) was calculated (Table 2).

The coefficients for the contributing and triggering factors in the landslide susceptibility models show differences between triggers and different sizes of landslides. Curvature, altitude and slope gradient have a high impact on the susceptibility of RTL, while curvature, PGA, relative relief, and slope gradient have high impact on susceptibility of ETL. The size classes of RTL show larger differences in weight of curvature, relative relief and altitude. For ETL the difference between size classes are largest for factors of PGA, curvature, and relative relief.

294

295

296

297

298

299

300

301

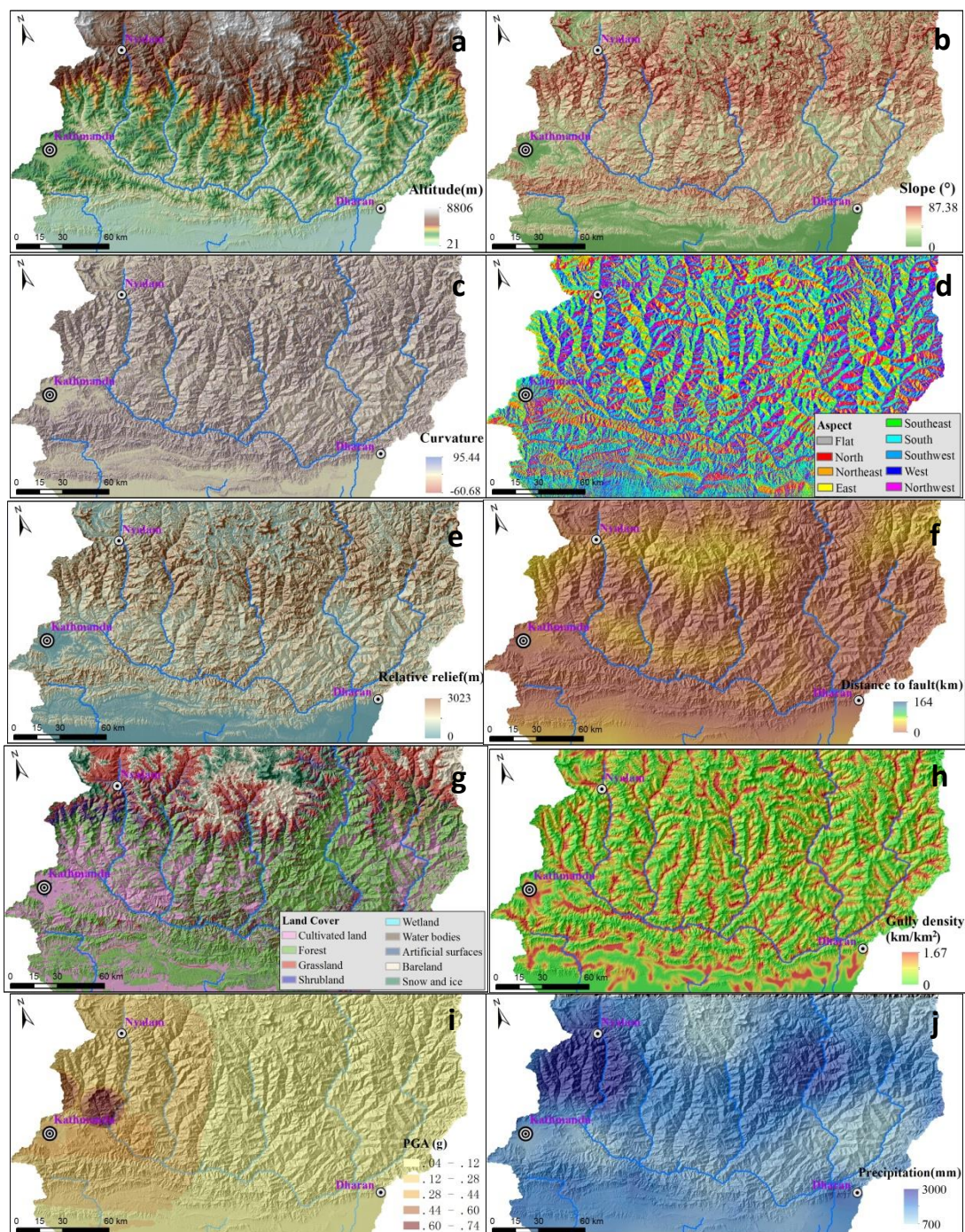


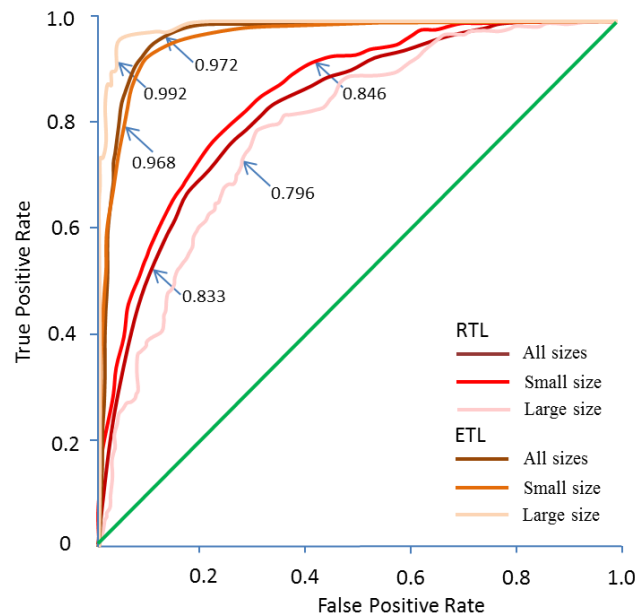
Fig. 7 Landslide susceptibility assessing factors; a: altitude(Data source: JAXA/METI ALOS PALSAR DEM); b: slope gradient; c: slope curvature; d: slope direction; e: relative relief; f: distance to fault; g: land cover; h: drainage density; i: Peak Ground Acceleration of the 2015 Gorkha earthquake (Peak Ground Acceleration data for the Gorkha earthquake

302 were obtained from USGS Shakemap, which was designed as a rapid response tool to portray the extent and variation
 303 of ground shaking throughout the affected region immediately following significant earthquakes); j: Average total
 304 monsoon precipitation (ICIMOD and the National Meteorological information Center of China. This data is the
 305 average precipitation for the period 1991-2010, for the monsoon season from June to October).

307 **Table 2** Susceptibility models for different triggers and landslide size classes in the Koshi River basin

Landslide type	x ₁	x ₂	x ₃	x ₄	x ₅	x ₆	x ₇	x ₈	x ₉	x ₁₀	p
All RTL	-6.4317	6.4955	-12.2440	-0.1717	-3.7048	-1.3431	1.0590	-0.7090	1.3725	0.7206	4.3961
Small size RTL	-8.36420	6.33158	-1.37934	-0.09899	-2.68158	-1.91514	1.10489	-0.93464	1.10003	0.98897	-0.54775
Large size RTL	-4.93126	6.47043	7.03034	-0.30706	4.79661	-0.13525	1.49649	-0.49201	1.31034	0.07492	-6.69787
All ETL	-3.3342	5.8510	-8.6844	-0.5513	8.8514	6.3296	3.2108	-0.2472	1.3740	17.4360	-6.4566
Small size ETL	-7.4433	5.8410	-7.5233	-0.1974	5.9871	4.2647	2.6977	1.7495	1.2858	7.5676	-3.3845
Large size ETL	6.939	10.116	-26.355	3.660	16.503	11.678	3.962	-4.039	2.633	28.199	-11.445

308
 309 ROC curves were drawn to verify the accuracy of each susceptibility model (Fig. 8), and the Area Under Curve (AUC)
 310 was calculated. The AUC values of the ETL models were higher than for RTL, since the ETL were more concentrated
 311 than the RTL, as the inventory is from one single triggering event, whereas the RTLs are from many different rainfall
 312 events over a longer time period.



313
 314 **Fig. 8** ROC curves for the susceptibility assessing models to different sizes of RTL and ETL

315

316 6.2 Results

317 The logistic regression models were employed to the Koshi River basin and in total six susceptibility maps were
318 generated (Fig. 9). Susceptibility values were classified into four levels: low, moderate, high and very high, based on
319 the following susceptibility threshold values: 0-0.25, 0.25-0.5, 0.5-0.75 and 0.75-1.

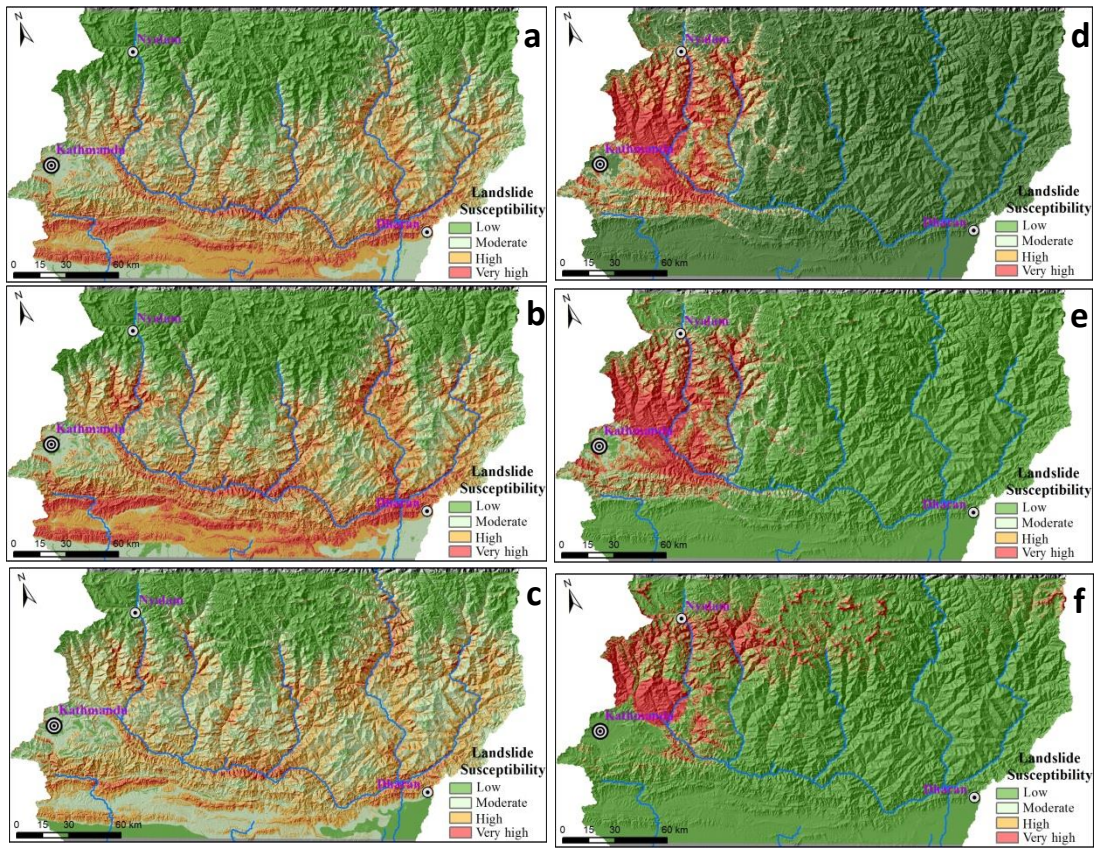
320 The RTL susceptibility map (Fig. 9a) shows that high and very high susceptible are located mostly in the Siwaliks and
321 in the Mahabharat Lekh region in west-eastern direction and the Middle to High Himalaya region in north-south
322 direction. The Siwaliks and Mahabharat Lekh regions (Fig. 1) have high and very high susceptibility levels for small
323 landslides, and lower susceptibility levels for large ones. The Middle and High Himalaya region (Fig. 1) has a reverse
324 situation: high and very high susceptibility levels for large landslides, and lower levels for small ones.

325 The ETL susceptibility map reflects the co-seismic landslide pattern of the Gorkha earthquake, with very high and high
326 susceptibility in the western part of the Koshi River basin. It is important to note that the ETL susceptibility map only
327 reflects the characteristics of the Gorkha earthquake and is therefore not a reliable map for future earthquakes that may
328 have another epicentral location, length of fault ruptures and magnitudes.

329 Both ETL and RTL susceptibility maps show different patterns for the large size landslide class (Fig. 9 c and f),
330 whereas the maps for small size (Fig. 9 b and e) resemble those of all size classes (Fig. 9 a and d). This is due to the
331 relative small fraction of the large size landslides in comparison with the small ones, and their more restricted location,
332 which gives different weight values for some factor maps (Table 2).

333 The highest susceptibility zones for small size and large size RTL show a large overlapping area, although the area of
334 these classes is much smaller for large size RTL. In the Siwaliks and Mahabharat Lekh regions high and very high
335 susceptibility zones for large size RTL are located in the upper steep hillslopes. In the Middle and High Himalaya
336 region, the highest susceptibility zones for both small size and large size RTL are mostly located on steep slopes along
337 rivers. The highest susceptibility zones for both small and large size ETL are located in the northwestern part of the
338 Koshi basin. For large size ETL these are concentrated in a smaller area to the northeast of Kathmandu (with altitude
339 higher than 3000m) where small ETL also show high susceptibility in the southeast of Kathmandu.

340



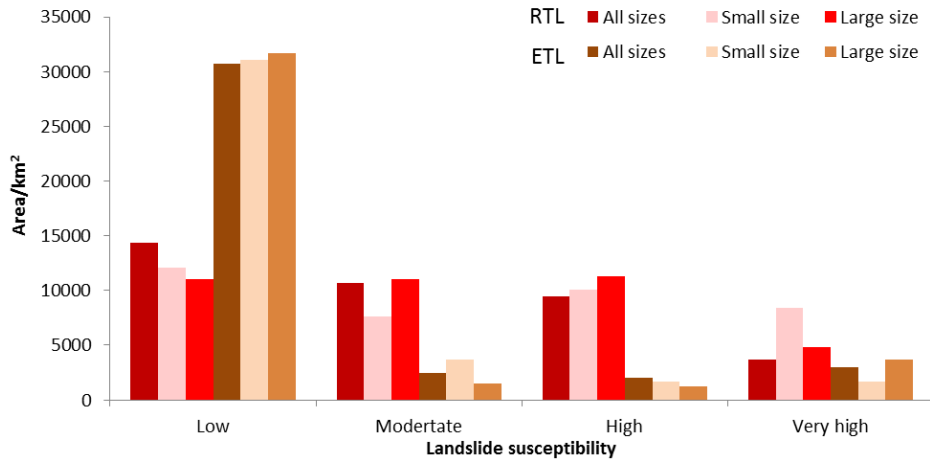
341

342 **Fig. 9** Susceptibility maps for different sizes of RTL and ETL: (a) for all RTLs; (b) for small RTLs; (c) for large RTLs; (d) for
 343 all ETLs; (e) for small ETLs; (f) for large ETLs.

344

345 The areal coverage of the landslide susceptibility classes was calculated for each susceptibility map (Fig. 10).
 346 Compared to RTL, the ETL susceptibility maps have a larger area with low susceptibility, due to fact that the Koshi
 347 River basin is far from the epicenter of Gorkha earthquake, thus the earthquake affected region is only part of the
 348 basin. The very high and high susceptible region for ETL is mostly concentrated in the western and southwestern parts
 349 of the basin, clearly reflecting the PGA pattern (Fig. 7i). The RTL susceptibility also reflects the triggering factor
 350 (monsoonal rainfall), with the highest susceptibility in the south of the basin. However, the higher rainfall peak in the
 351 Middle and High Himalaya region is less pronounced in the susceptibility maps, as well as in the inventory maps (Fig.
 352 4). The higher susceptibility classes for large ETL occupy more area than for small ETL, while the opposite can be
 353 observed for RTL.

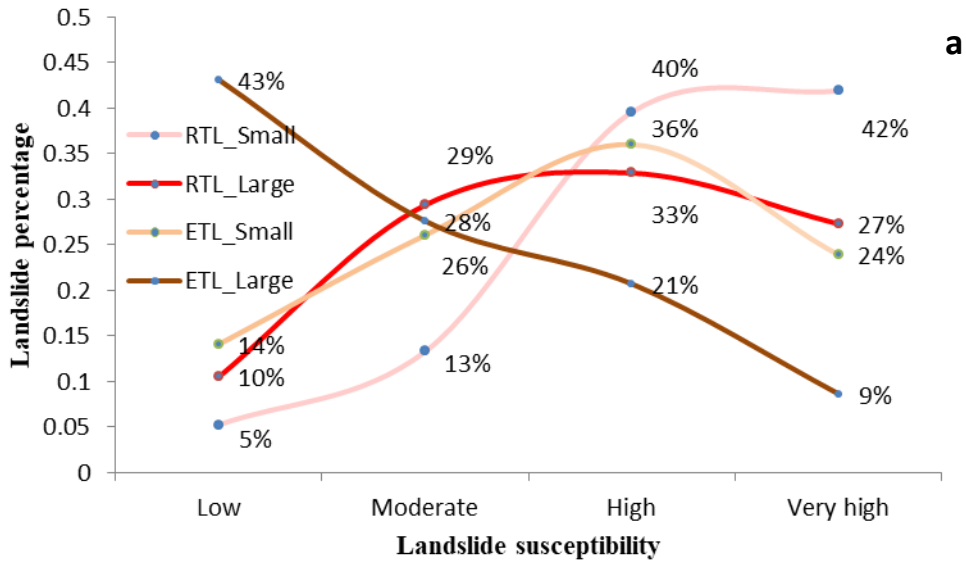
354



355
356 **Fig. 10** Coverage of different landslide susceptibility classes for ETL and RTL maps
357

358 **7. Validation of landslide susceptibility maps**

359 Different groups of landslide data were used to validate the landslide susceptibility maps for RTL and ETL. For each
360 trigger and size class, the number of landslides was calculated, inside the areas with a certain susceptibility level, to
361 cross-validate the results.
362



363

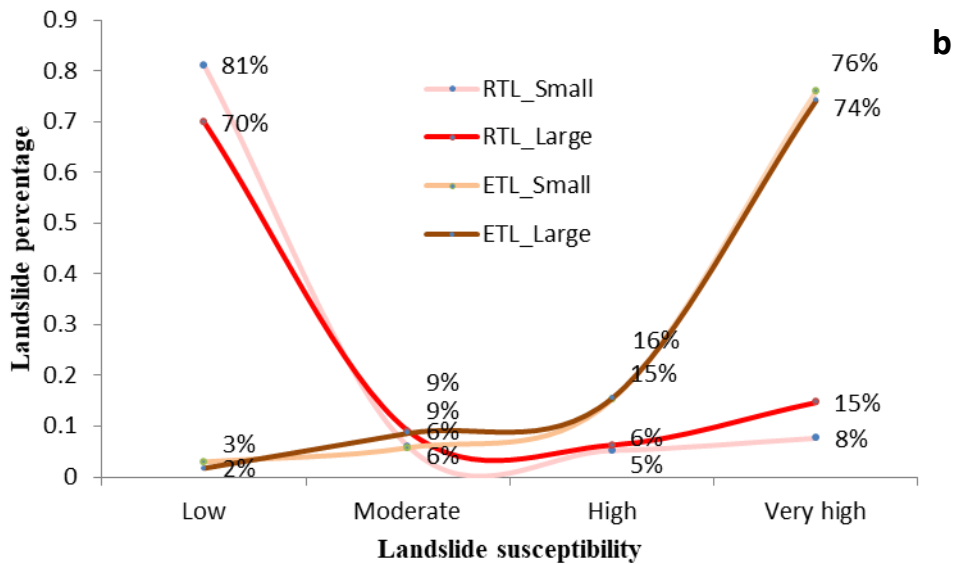


Fig. 11 Cross validation of the landslide susceptibility maps. (a) The percentage of landslides in the various classes of the RTL susceptibility map; (b) The percentage of landslides in the various classes of the ETL susceptibility map.

The percentages of different size RTLs and ETLs in each susceptibility are shown in Fig.11. For the RTL susceptibility map, percentages of of small size and large size landslides show a similar tendency, for both triggers. Most of the landslides were located in high and very high susceptibility zones. Only large size of ETL shows an opposite trendency. There is a marked difference between the percentages of ETL and RTL in the ETL landslide susceptibility classes. the RTL and ETL percentages show completely different patterns. Most of the RTLs (both small and large) are located in the low ETL susceptible regions. Conversely, a large fraction of small size and large size of ETLs are located in the high susceptible regions.

8. Discussion

This study aimed to analyze independent rainfall- (RTL) and earthquake-triggered landslide (ETL) inventories for a large mountainous watershed in the Himalayas, located in India, Nepal and China. It is important to mention, that the two rainfall-triggered landslide inventories are not event-based inventories (Guzzetti et al., 2012). A major limitation in this work was that we were not able to use separate event-based inventories for RTLs, and only one event-based inventory for ETL. The collection of event-based inventories, both for rainfall and earthquake triggers, remains one of the main challenges in order to advance the study of landslide hazard at a watershed scale. Another limitation for this landslide inventory was that, the temporal and quality of high resolution images, as well as revegetation affects the number of historic landslide inventory. More and more researchers make great efforts on the event-based landslide

385 inventories and database (Marc et al., 2018), which may supply more samples for comparison studies of RTL and ETL.
386 The two RTL inventories differ in the sense that the 1992 inventory is based on landslides that were large enough to be
387 mapped on the topographic map, where as the inventory between 1992 and 2015 represents the landslides that could be
388 mapped from multi-temporal images over a number of years. Both inventories were lacking a separation into initiation
389 and accumulation parts, and no separation in landslide types could be made. The effects of amalgamation of landslides
390 might certainly have played a role in the Frequency Area Distribution (Marc and Hovius, 2015) although we are not
391 able to quantify this, due to lack of an independent dataset. For the 1992-2015 dataset we were able to control this as
392 we carried out the image interpretation ourselves, but the pre-1992 inventory could not be verified as the aerial
393 photographs that were used to generate the updated topographic maps, were not available to us. Although the two
394 inventories differ substantially with respect to the number of small landslides, it is striking to see that the cut-off
395 values, and β values in the Frequency Area Distribution (FAD) are similar. It is very difficult to obtain a complete
396 event-based landslide inventory for rainfall triggered landslides in Nepal, as landslides are generally generated by a
397 number of extreme rainfall events during the monsoon, which can not be separated, as the area is cloud-covered
398 through most of the period. The earthquake triggered landslide distribution is an event-based inventory, for a single
399 earthquake (2015 Gorkha) and based on an extensive mapping effort by Roback et al. (2017) resulting in an inventory
400 that can be considered as complete (Tanyas et al., 2017a). When comparing the FAD for RTL and ETL it is striking
401 that the size-frequency distributions for both ETL and RTL show very similar behaviour for landslides above the cut-
402 off value of 30,000 m². Although there is no consensus regarding the factors dictating the power-law distribution of
403 landslides, there is an accumulating evidence that topography, as well as mechanical properties, has to be one of an
404 important controlling factors (e.g., Stark and Guzzeti, 2009; ten Brink et al., 2009; Frattini and Crosta, 2013; Liucci et
405 al., 2017). Our finding regarding similar cutoff values obtained from different inventories created for the same area is
406 also supporting this argument. This conclusion also supported by Marc et al., 2019, who found that similar Beta values
407 between ETL and RTL, but the cutoff value is much smaller because a correction to remove runoff was applied.
408

409 9. Conclusions

410 The pattern of the triggers (precipitation in the Monsoon for RTL, and PGA distribution for ETL) have major influence
411 on the distribution of landslides and susceptibility zones. These trigger patterns differ substantially. When moist
412 airflow from the India Ocean crosses over the Mahabharat Lekh, the intensity of precipitation reduces because the
413 altitude lowers and temperature rises. As the airflow continues northwards to the Middle Mountains and Transition
414 Belt, it rises again and consequently induces high precipitation in the area at an altitude between 2500~4000m. It
415 results in two high precipitation regions during the monsoon season (Fig.7 i), which are reflected in the zones of high
416 susceptibility to RTL. The precipitation pattern is different from the PGA distribution (Fig.7 j) for the Gorkha

417 earthquake, with strong shaking area located in the North and North east of Kathmandu, with PGA values larger than
418 0.44g. One limitation need to be clarified that, normally the rainfall on the day of the land sliding event and antecedent
419 daily rainfall, which have close correlation with landslide occurrence, are usually taken as the key factors for landslide
420 threshold. But in this study the mean precipitation during monsoon season were taken as the rainfall factor. It could be
421 only supply a general tendency for landslide distribution in regional scale. In the RTL susceptibility assessment model,
422 the weight of precipitation factor is low, which means this factor was not strong correlated with landslide susceptibility.
423 It is better to characterize the variability of daily rainfall during the monsoon season, and take into account the daily
424 rainfall instead of the mean. So use the short-term rainfall variability to study the long term historical landslide
425 inventory and susceptibility assessment may be more reasonable (Deal et al., 2017).

426 The distribution of RTL and ETL susceptibility classes are also very different. As the ETL susceptibility map is based
427 on a single event, the distribution of the susceptibility classes is controlled by the PGA for the 2015 Gorkha
428 earthquake, and the patterns of the ETL susceptibility map differs from the RTL susceptibility map. This was
429 confirmed by the cross validation (Fig. 11), which showed that the RTL susceptibility map has a modest capability of
430 explaining the ETL pattern, but that the ETL susceptibility cannot properly predict the RTLs.

431 This means one should be careful with using susceptibility maps that were made for earthquake induced landslides, as
432 prediction tools for rainfall induced landslides. Such maps are in fact of little practical implication, as the next
433 earthquake may not be likely to occur in the same location and therefore produce a similar landslide pattern. The
434 generation of ETL susceptibility maps should not be based on single earthquake scenario scenarios (Jibson, 2011), and
435 ideally many earthquake scenarios should be used to model the overall ETL susceptibility. However, using PGA values
436 based on probabilistic seismic hazard assessment might result is relatively poor statistical correlations with event-based
437 inventories. Therefore, PGA maps and ETL inventories of specific earthquake scenarios are required to improve the
438 statistical models. This requires more event-based ETL inventores, and efforts to generate worlwide digital databases
439 should be encouraged (Tanyas et al., 2017a).

440 The relationship between ETL and RTL might also change over time. Rainfall-induced landslide activity is generally
441 much higher in the first years after an earthquake, and generally decreases to pre-earthquake levels within a decade,
442 due to depletion of co-seismic sediments, progressive coarsening of available sediments and revegetation (Fan et al.,
443 2018b; Hovius et al., 2011; Marc et al., 2015). Landslide susceptibility map should also be updated after major
444 earthquakes.

445 Both ETL susceptibility maps and RTL susceptibility maps show different patterns for large landslides, as compared to
446 the small landslide or all landslides. In general the susceptibility maps, for both RTL and ETL, for all landslide sizes
447 together show a large similarity with the ones for the small landslides only. This is due to the fact that the number of
448 large landslides is quite limited as compared to the small landslides (See Table 1), and the samples used for generation

449 the models for all landslides and only small landslides are almost the same. However, the resulting susceptibility
450 patterns are quite different, and it is therefore questionable whether landslide susceptibility maps that are generated for
451 all landslide size would be able to accurately predict the large landslides. More emphasis should be given to the
452 evaluation of landslide size in susceptibility and subsequent hazard and risk assessment. This is relevant for analyzing
453 the potential runout areas of landslides and for evaluation landslide damming susceptibility (Fan et al., 2014; 2018b).
454 Therefore, size and trigger matter in landslide susceptibility assessment.

455

456 **10. Acknowledgements**

457 This research was supported by the National Natural Science Foundation of China (Grant No.41401007), the External
458 Cooperation Program of BIC, Chinese Academy of Sciences (Grant No. 131551KYSB20130003) and the “135”
459 Program of IMHE (Grant No. SDS-135-1708). This study was also jointly supported by the Australian government
460 funded Koshi Basin Programme at ICIMOD as well as ICIMOD’s core funds contributed by the governments of
461 Afghanistan, Australia, Austria, Bangladesh, Bhutan, China, India, Myanmar, Nepal, Norway, Pakistan, Switzerland,
462 and the United Kingdom.

463

464

465 **References**

- 466 Ayalew, L., and Yamagishi, H.: The application of GIS-based logistic regression for landslide susceptibility mapping in
467 the Kakuda-Yahiko Mountains, Central Japan. *Geomorphology*, 65(1–2), 15–31,
468 <https://doi.org/10.1016/j.geomorph.2004.06.010>, 2005.
- 469 Bai, S., Wang, J., Lü, G. N., Zhou, P. G., Hou, S. S., and Xu, S.N.: GIS-based logistic regression for landslide
470 susceptibility mapping of the Zhongxian segment in the Three Gorges area, China, *Geomorphology*, 115(1–2),
471 23–31, <https://doi.org/10.1016/j.geomorph.2009.09.025> , 2010.
- 472 Burg, J.P., Guiraud, M., Chen, G.M., and Li, G.C.: Himalayan metamorphism and deformations in the North
473 Himalayan Belt (southern Tibet, China), *Earth Planet Sci Lett*, 69, 391–400, [https://doi.org/10.1016/0012-](https://doi.org/10.1016/0012-821x(84)90197-3)
474 [821x\(84\)90197-3](https://doi.org/10.1016/0012-821x(84)90197-3), 1984.
- 475 Chang, K.T., Chiang, S. H., and Hsu, M. L.: Modeling typhoon- and earthquake-induced landslides in a mountainous
476 watershed using logistic regression, *Geomorphology*, 89(3–4), 335–347,
477 <https://doi.org/doi:10.1016/j.geomorph.2006.12.011>, 2007.
- 478 Clauset, A., Shalizi, C. R., and Newman, M. E.: Power-law distributions in empirical data. *SIAM Review*, 51(4), 661–
479 703, <https://doi.org/10.1137/070710111>, 2009.

480 Collins, B. D., and Jibson, R. W.: Assessment of existing and potential landslide hazards resulting from the April 25,
481 2015 Gorkha, Nepal earthquake sequence. U.S. Geological Survey Open File Report 2015-1142, Reston, VA,
482 2015.

483 Dai, F. C., and Lee, C. F.: Frequency-volume relation and prediction of rainfall-induced landslides, *Engineering*
484 *Geology*, 59(3-4), 253-266, [https://doi.org/10.1016/S0013-7952\(00\)00077-6](https://doi.org/10.1016/S0013-7952(00)00077-6), 2001.

485 Dahal, R. K., and Hasegawa, S.: Representative rainfall thresholds for landslides in the Nepal Himalaya,
486 *Geomorphology*, 100 (3-4), 429–443, <https://doi.org/10.1016/j.geomorph.2008.01.014>, 2008.

487 Das, I., Sahoo, S., van Westen, C. J., Stain, A., and Hack, R.: Landslide susceptibility assessment using logistic
488 regression and its comparison with a rock mass classification system, along a road section in the northern
489 Himalayas (India), *Geomorphology*, 114(4), 627-637, <https://doi.org/10.1016/j.geomorph.2009.09.023>, 2000.

490 Deal, E., Favre, A. C., and Braun, J.: Rainfall variability in the Himalayan orogen and its relevance to erosion
491 processes, *Water Resources Research*, 53(5), 4004-4021, <https://doi.org/10.1002/2016WR020030>, 2017.

492 Dhital, M. R.: *Geology of the Nepal Himalaya, Regional Perspective of the Classic Collided Orogen*, Springer,
493 Switzerland, <https://doi.org/10.1007/978-3-319-02496-7>, 2015.

494 Dilley, M., Chen, R. S., Deichmann, U., Lerner-Lam, A. L., and Arnold, M. Natural disaster hotspots: a global risk
495 analysis, The World Bank Hazard Management Unit, Washington, 2005.

496 Fawcett, T.: An introduction to ROC analysis, *Pattern Recognition Letters* 27, 861–874,
497 <https://doi.org/10.1016/j.patrec.2005.10.010> 2006.

498 Fan, X., Qiao, J., Han, M., and Zeng, Y.: Volumes and movement distances of earthquake and rainfall-induced
499 catastrophic landslides, *Rock and Soil Mechanics*, 33(10), 3051-3058, 2012.

500 Fan, X., Rossiter, D. G., van Westen, C. J., Xu, Q., and Görüm, T.: Empirical prediction of coseismic landslide dam
501 formation: coseismic landslide dam formation, *Earth Surf. Process. Landf.*, 39, 1913–1926,
502 <https://doi.org/10.1002/esp.3585>, 2014.

503 Fan, X., Domènech, G., Scaringi, G., Huang, R., Xu, Q., Hales, T. C., Dai, L., Yang, Q., and Francis, O.: Spatio-
504 temporal evolution of mass wasting after the 2008 Mw 7.9 Wenchuan Earthquake revealed by a detailed multi-
505 temporal inventory, *Landslides*, <https://doi.org/10.1007/s10346-018-1054-5>, 2018a.

506 Fan, X., Juang, C.H., Wasowski, J., Huang, R., Xu, Q., Scaringi, G., van Westen, C.J., and Havenith, H. –B.: What we
507 have learned from the 2008 Wenchuan Earthquake and its aftermath: A decade of research and challenges, *Eng.*
508 *Geol.*, 241, 25–32, <https://doi.org/10.1016/j.enggeo.2018.05.004>, 2018b.

509 Frattini, P., and Crosta, G. B.: The role of material properties and landscape morphology on landslide size distributions,
510 *Earth and Planetary Science Letters*, 361, 310-319, <https://doi.org/10.1016/j.epsl.2012.10.029>, 2013.

511 Froude, M. J., and Petley, D. N.: Global fatal landslide occurrence from 2004 to 2016, *Natural Hazards and Earth*

512 System Sciences, 18: 2161-2181, <https://doi.org/10.5194/nhess-18-2161-2018>, 2018.

513 Gansser, A.: *Geology of the Himalayas*, Interscience, New York, 1964.

514 Gurung, H. B., and Khanal, N. R.: *Landscape processes in the Chure range*, Nepal National Committee for Man and
515 the Biosphere, Kathmandu, 1987.

516 Guzzetti, F., Ardizzone, F., Cardinali, M., Rossi, M., and Valigi, D.: Landslide volumes and landslide mobilization
517 rates in Umbria, central Italy, *Earth and Planetary Science Letters*, 279(3-4), 222-229,
518 <https://doi.org/10.1016/j.epsl.2009.01.005>, 2008.

519 Guzzetti, F., Mondini, A. C., Cardinali, M., Fiorucci, F., Santangelo, M., and Chang, K. -T.: Landslide inventory
520 maps: New tools for an old problem, *Earth-Science Reviews*, 112(1-2), 42-66,
521 <https://doi.org/10.1016/j.earscirev.2012.02.001>, 2012.

522 Haque, U., Blum, P., da Silva, P. F., Andersen, P., Pilz, J., Chalov, S. R., Malet, J. -P., Auflič, M. J., Andres, N.,
523 Royiadji, E., Lamas, P. C., Zhang, W., and Peshevski, I.: Fatal landslides in Europe, *Landslides*, 13(6), 1545-
524 1554, <https://doi.org/10.1007/s10346-016-0689-3>, 2016.

525 Highland, L. M., and Bobrowsky, P.: *The landslide handbook-A guide to understanding landslides*: Reston, Virginia,
526 U.S. Geological Survey Circular 1325, 129 p., 2008.

527 Hodges, K. V., Parrish, R. R. and Searle, M. P.: Tectonic evolution of the central Annapurna Range, Nepalese
528 Himalaya, *Tectonics*, 15, 1264-1291, 1996.

529 Hovius, N., Stark, C. P., and Allen, P. A.: Sediment flux from a mountain belt derived by landslide mapping, *Geology*
530 25(3), 231-234, [https://doi.org/10.1130/0091-7613\(1997\)025<0231:SFFAMB>2.3.CO;2](https://doi.org/10.1130/0091-7613(1997)025<0231:SFFAMB>2.3.CO;2), 1997.

531 Hovius, N., Stark, C. P., Chu, H. T., and Lin, J. C.: Supply and removal of sediment in a landslide-dominated mountain
532 belt: Central Range, Taiwan, *The Journal of Geology*, 108(1), 73-89, <https://doi.org/10.1086/314387>, 2000.

533 Hovius, N., Meunier, P., Lin, C. W., Chen, H., Chen Y. G., Dadson, S. J., Horng, M. J., and Lines, M.: Prolonged
534 seismically induced erosion and the mass balance of a large earthquake, *Earth Planet. Sci. Lett.*, 304, 347-355,
535 <https://doi.org/10.1016/j.epsl.2011.02.005>, 2011.

536 Hussin, H. Y., Zumpano, V., Reichenbach, P., Sterlacchini, S., Micu, M., van Westen, C. J., and Balteanu, D.: Different
537 landslide sampling strategies in a grid - based bi - variate statistical susceptibility model, *Geomorphology*, 253,
538 508-523, <https://doi.org/10.1016/j.geomorph.2015.10.030>, 2016.

539 Jibson, R. W.: Methods for assessing the stability of slopes during earthquakes-A retrospective, *Eng. Geol.*, 122, 43-
540 50, 2011.

541 Kargel, J. S., Leonard, G. J., Shugar, D. H., Haritashya, U. K., Bevington, A., Fielding, E. J., Fujita, K., Geertsema, M.,
542 Miles, E. S., Steiner, J., Anderson, E., Bajracharya, S., Bawden, G. W., Breashears, D. F., Byers, A., Collins, B.,
543 Dhital, M. R., Donnellan, A., Evans, T. L., Geai, M. L., Glasscoe, M. T., Green, D., Gurung, D. R., Heijenk, R. ,

544 Hilborn, A., Hudnut, K., Huyck, C., Immerzeel, W. W., Jiang, L., Jibson, R., Kääb, A., Khanal, N. R.,
545 Kirschbaum, D., Kraaijenbrink, P. D. A., Lamsal, D., Shiyin, L., Lv, M., McKinney, D., Nahirnick, N. K.,
546 Nan, Z., Ojha, S., Olsenholler, J., Painter, T. H., Pleasants, M., Pratima, K. C., Yuan, Q. I., Raup, B. H.,
547 Regmi, D., Rounce, D. R., Sakai, A., Donghui, S., Shea, J. M., Shrestha, A. B., Shukla, A., Stumm, D., van
548 der Kooij, M., Voss, K., Xin, W., Weihs, B., Wolfe, D., Wu, L., Yao, X., Yoder, M. R., and Young, N.:
549 Geomorphic and geologic controls of geohazards induced by Nepal's 2015 Gorkha earthquake, *Science*, 351,
550 aac8353, <https://doi.org/10.1126/science.aac8353>, 2, 2016.

551 Keefer, D. K.: Investigating landslides caused by earthquakes—a historical review, *Surv. Geophys.*, 23, 473-510,
552 <https://doi.org/10.1023/A:1021274710840>, 2002.

553 Kirschbaum, D., Stanley, T., and Zhou, Y.: Spatial and temporal analysis of a global landslide catalog, *Geomorphology*,
554 249, 4-15, <https://doi.org/10.1016/j.geomorph.2015.03.016>, 2015.

555 Klar, A., Aharonow, E., Kalderon-Asael, B., and Katz, O.: Analytical and observational relations between landslide
556 volume and surface area, *Journal of Geophysical Research* 116(F2), 1-10.
557 <https://doi.org/10.1029/2009JF001604>, 2011.

558 Korup, O., Clague, J. J., Hermanns, R. L., Hewitt, K., Strom, A. L., and Weidinger, J. T.: Giant landslides topography
559 and erosion, *Earth Planet. Sci. Lett.*, 261(3), 578 – 589, <https://doi.org/10.1016/j.epsl.2007.07.025>, 2007.

560 Larsen, I. J., and Montgomery, D.R.: Landslide erosion coupled to tectonics and river incision. *Nature Geoscience*
561 5(7), 468–473. <https://doi.org/10.1038/ngeo1479>, 2012.

562 Larsen, I. J., Montgomery, D. R., and Korup, O.: Landslide erosion controlled by hillslope material, *Nature Geoscience*
563 3(4), 247-251, <https://doi.org/10.1038/ngeo776>, 2011.

564 Li, G., West, A. J., Densmore, A. L., Jin, Z., Parker, R. N., and Hilton, R. G.: Seismic mountain building: Landslides
565 associated with the 2008 Wenchuan earthquake in the context of a generalized model for earthquake volume
566 balance, *Geochem. Geophys. Geosyst.*, 15, 833–844, <https://doi.org/10.1002/2013GC005067>, 2014.

567 Lin, C. W., Liu, S. H., Lee, S. Y., Liu, C. C.: Impacts of the Chi-Chi earthquake on subsequent rainfall-induced
568 landslides in central Taiwan, *Engineering Geology*, 86(2-3): 87–101,
569 <https://doi.org/10.1016/j.enggeo.2006.02.010>, 2006.

570 Lin, G. W., Chen, H., Hovius, N., Horng, M. J., Dadson, S., Meunier, P., and Lines, M.: Effects of earthquake and
571 cyclone sequencing on landsliding and fluvial sediment transfer in a mountain catchment, *Earth Surf. Proc.*
572 *Land.*, 33, 1354-1373, <https://doi.org/10.1002/esp.1716>, 2008.

573 Liucci, L., Melelli, L., Suteanu, C., and Ponziani, F.: The role of topography in the scaling distribution of landslide
574 areas: A cellular automata modeling approach, *Geomorphology*, 290, 236-249,
575 <https://doi.org/10.1016/j.geomorph.2017.04.017>, 2017.

576 Pellicani, R., and Spilotro, G.: Evaluating the quality of landslide inventory maps: comparison between archive and
577 surveyed inventories for the Daunia region (Apulia, Southern Italy), *Bulletin of Engineering Geology and the*
578 *Environment*, 74(2), 357-367, <https://doi.org/10.1007/s10064-014-0639-z>, 2015.

579 Peng, L., Xu, S., Peng, J.: Research on development characteristics and size of landslide in the Three Gorges area,
580 *Geoscience*, 28(5): 1077-1086, 2014.

581 Petley, D.: Global patterns of loss of life from landslides, *Geology*, 40, 927–930, <https://doi.org/10.1130/G33217.1>,
582 2012.

583 Malamud, B. D., Turcotte, D. L., Guzzetti, F., and Reichenbach, P.: Landslide inventories and their statistical
584 properties, *Earth Surf. Process, Landform*, 29, 687-711, <https://doi.org/10.1002/esp.1064>, 2004.

585 Marc, O., Behling, R., Andermann, C., Turowski, J. M., Illien, L., Roessner, S., and Hovius, N.: Long-term erosion of
586 the Nepal Himalayas by bedrock landsliding: the role of monsoons, earthquakes and giant landslides, *Earth*
587 *Surf. Dynam.*, 7, 107-128, <https://doi.org/10.5194/esurf-7-107-2019>, 2019.

588 Marc, O., and Hovius, N.: Amalgamation in landslide maps: effects and automatic detection, *Nat. Hazards Earth Syst.*
589 *Sci.*, 15:723–733, <https://doi.org/10.5194/nhessd-2-7651-2014>, 2015.

590 Marc, O., Hovius, N., Meunier P., Uchida, T., and Hayashi, S.: Transient changes of landslide rates after earthquakes,
591 *Geology*, 43, 883–886, <https://doi.org/10.1130/G36961.1>, 2015.

592 Marc, O., Stumpf, A., Malet, J. -P., Gosset, M., Uchida, T., and Chiang, S. -H.: Initial insights from a global database
593 of rainfall-induced landslide inventories: the weak influence of slope and strong influence of total storm rainfall,
594 *Earth Surf. Dynam.*, 6, 903-922, <https://doi.org/10.5194/esurf-6-903-2018>, 2018.

595 Martha, T. R., Reddy, P. S., Bhatt, C. M., Govindha, Raj K.B., Nalini, J., Padmanabha, A., Narender, B., Kumar, K. V.,
596 Muralikrishnan, S., Rao, G. S., Diwakar, P. G., and Dadhwal, V. K.: Debris volume estimation and monitoring
597 of Phuktal river landslide-dammed lake in the Zaskar Himalayas, India using Cartosat-2 images, *Landslides*,
598 14(1), 373-383, <https://doi.org/10.1007/s10346-016-0749-8>, 2017a.

599 Martha, T. R., Roy, P., Mazumdar, R., Govindharaj, K. B., and Kumar, K. V.: Spatial characteristics of landslides
600 triggered by the 2015 Mw 7.8 (Gorkha) and Mw 7.3 (Dolakha) earthquakes in Nepal, *Landslides*, 14(2), 697–
601 704, <https://doi.org/10.1007/s10346-016-0763-x>, 2017b.

602 Meunier, P., Hovius, N., and Haines, J. A.: Topographic site effects and the location of earthquake induced landslides,
603 *Earth and Planetary Science Letters*, 275(3-4), 221-232, <https://doi.org/10.1016/j.epsl.2008.07.020>, 2008.

604 Nandi, A., and Shakoor, A.: A GIS-based landslide susceptibility evaluation using bivariate and multivariate statistical
605 analyses, *Engineering Geology*, 110(1–2), 11-20, <https://doi.org/10.1016/j.enggeo.2009.10.001>, 2010.

606 Razavizadeh, S., Solaimani, K., Massironi, M. and Kavian, A.: Mapping landslide susceptibility with frequency ratio,
607 statistical index, and weights of evidence models: a case study in northern Iran, *Environmental Earth Sciences*,

608 76(14), 499, <https://doi.org/10.1007/s12665-017-6839-7>, 2017.

609 Reichenbach, P., Rossi, M., Malamud, B. D., Mihir, M. and Guzzetti, F.: A review of statistically-based landslide
610 susceptibility models, *Earth-Science Reviews*, 180, 60-91, <https://doi.org/10.1016/j.earscirev.2018.03.001> ,
611 2018.

612 Roback, K., Clark, M. K., West, A. J., Zekkos, D., Li, G., Gallen, S. F., Champlain, D., and Godt, J. W.: Map data of
613 landslides triggered by the 25 April 2015 Mw 7.8 Gorkha, Nepal earthquake: U.S. Geological Survey data
614 release, <https://doi.org/10.5066/F7DZ06F9>, 2017.

615 Saba, S. B., van der Meijde, M., and van der Werff, H.: Spatio-temporal landslide detection for the 2005 Kashmir
616 earthquake region, *Geomorphology*, 124(1-2), 17-25, <https://doi.org/10.1016/j.geomorph.2010.07.026>, 2010.

617 SafeLand: Guidelines for landslide susceptibility, hazard and risk assessment and zoning,
618 <https://www.ngi.no/eng/Projects/SafeLand>, 2015.

619 Stark, C. P. and Guzzetti, F.: Landslide rupture and the probability distribution of mobilized debris volumes, *J.*
620 *Geophys. Res.-Earth*, 114, F00A02, <https://doi.org/10.1029/2008JF001008>, 2009.

621 Stark, C. P., and Hovius, N.: The characterization of landslide size distributions, *Geophysical Research Letters*, 28,
622 1091-1094, <https://doi.org/10.1029/2000GL008527>, 2001.

623 Tang, C., Zhu, J., and Qi, X.: Landslide hazard assessment of the 2008 Wenchuan earthquake: a case study in Beichuan
624 area, *Canadian Geotechnical Journal*, 48(1), 128-145, <https://doi.org/10.1139/T10-059>, 2010.

625 Tang, C., van Westen, C. J., Tanyas, H., and Jetten, V. G.: Analysing post-earthquake landslide activity using multi-
626 temporal landslide inventories near the epicentral area of the 2008 Wenchuan earthquake, *Nat. Hazards Earth*
627 *Syst. Sci.*, 16,2641-2655, <https://doi.org/10.5194/nhess-16-2641-2016>, 2016.

628 Tanyas, H., van Westen, C. J., Allstadt, K. E., Jesse, M. A., Gorum, T., Jibson, R. W., Godt, J. W., Sato, H. P., Schmidt,
629 R. G., Marc, O., and Hovius, N.: Presentation and Analysis of a World-Wide Database of Earthquake-Induced
630 Landslide Inventories, *Journal of Geophysical Research, Earth Surface*, 122, 1991-2015,
631 <https://doi.org/10.1002/2017jf004236> , 2017a.

632 Tanyas, H., Allstadt, K. E., and van Westen, C. J.: An updated method for estimating landslide-event magnitude, *Earth*
633 *Surface Processes and Landforms*, <https://doi.org/10.1002/esp.4359>, 2017b.

634 ten Brink, U. S., Barkan, R., Andrews, B. D., and Chaytor, J. D.: Size distributions and failure initiation of submarine
635 and subaerial landslides, *Earth and Planetary Science Letters* 287: 31-42,
636 <https://doi.org/10.1016/j.epsl.2009.07.031>, 2009.

637 Tong, L., Qi, S., An, G., and Liu, C.: Large scale geo-hazards investigation by remote sensing in Himalayan region,
638 Science Press, Beijing, 2013.

639 Wald, D. J., Quitoriano, V., Heaton, T. H., and Kanamori, H.: Relationship between Peak Ground Acceleration, Peak

640 Ground Velocity, and Modified Mercalli Intensity for Earthquakes in California, *Earthquake Spectra*,
641 <http://earthquake.usgs.gov/shakemap/global/shake/about.html#references>, 1999.

642 Wang, L., Sawada, K., and Moriguchi, S.: Landslide susceptibility analysis with logistic regression model based on
643 FCM sampling strategy, *Computers and Geosciences*, 57, 81-92, <https://doi.org/10.1016/j.cageo.2013.04.006>,
644 2013.

645 Zhang, J., Gurung, D. R., Liu, R. K., Murthy, M. S. R., and Su, F. H.: Abe Barek landslide and landslide susceptibility
646 assessment in Badakhshan Province, Afghanistan, *Landslides*, 12(3), 597-609, [https://doi.org/10.1007/s10346-](https://doi.org/10.1007/s10346-015-0558-5)
647 015-0558-5, 2015.

648 Zhang, J., Liu, R., Deng, W., Khanal, N. R., Gurung, D. R., Murthy, M. S. R., and Wahid, S.: Characteristics of
649 landslide in Koshi River basin, central Himalaya, *Journal of Mountain Science*, 13(10), 1711-1722,
650 <https://doi.org/10.1007/s11629-016-4017-0>, 2016.

651